Supplementary Materials
Giant Exciton Mott Density in Anatase TiO_2

Edoardo Baldini*,[1,2] Tania Palmieri,[1] Adriel Dominguez,[3,4,5] Angel Rubio,[6,7,8] and Majed Chergui†[1]

[1] *Laboratory of Ultrafast Spectroscopy, ISIC and Lausanne Centre for Ultrafast Science (LACUS), École Polytechnique Fédérale de Lausanne, CH-1015 Lausanne, Switzerland*
[2] *Department of Physics, Massachusetts Institute of Technology, 02139 Cambridge, Massachusetts, USA*
[3] *Bremen Center for Computational Material Science (BCCMS), Bremen, Germany*
[4] *Shenzhen JL Computational Science and Applied Research Institute (CSAR), Shenzhen, China*
[5] *Beijing Computational Research Center (CSRC), Beijing, China*
[6] *Max Planck Institute for the Structure and Dynamics of Matter, Hamburg, Germany*
[7] *Departamento Física de Materiales, Universidad del País Vasco, Av. Tolosa 72, E-20018, San Sebastian, Spain*
[8] *Center for Computational Quantum Physics, The Flatiron Institute, 162 Fifth Avenue, New York, NY 10010, USA*

(Dated: August 19, 2020)

* ebaldini@mit.edu † majed.chergui@epfl.ch

I. FIRST-PRINCIPLES CALCULATIONS

A. Electronic structure

The electronic structure of pristine and electron-doped anatase TiO_2 was calculated using many-body perturbation theory at the one-shot *GW* level [1]. This approach has been shown to describe accurately the electronic properties of many band semiconductors [2]. In the case of anatase TiO_2, the *GW* electronic band structure and gap size are in excellent agreement with those obtained from angle-resolved photoemission spectroscopy measurements [3].

The system was modelled by using the primitive unit cell of anatase TiO_2 with lattice parameters $a = b = 3.79$ $\mathring{A}$ and $c = 9.67$ $\mathring{A}$ (unit cell volume of 69.58 $\mathring{A}^3$). These values were calculated using the generalized gradient approximation (GGA), and are in line with the experimental values. The Brillouin zone was sampled with a 4×4×4 k-point grid. We used a total of 2474 conduction bands and a 46 Ry energy cutoff for the computation of the inverse dielectric matrix. An energy cutoff of 46 Ry and 160 Ry was employed for the evaluation of the screened and the bare Coulomb interaction components of the self-energy operator, respectively. All these parameters were systematically and independently increased until the obtained electronic structure was converged within few tens of meV (see Ref. [3] for a detailed discussion).

B. Optical response

We calculated the optical spectra with and without electron-hole (e-h) correlations, relying on the computed *GW* quasiparticle energies. In the case with no e-h correlations, we used the random phase approximation (RPA) and obtained a featureless optical spectrum that quantifies the contribution of the direct e-h continuum. In contrast, solving the Bethe-Salpeter equation (BSE) allowed us to capture the excitonic features observed in spectroscopic ellipsometry measurements both qualitatively and quantitatively [3]. To solve the BSE, we employed a 16×16×16 k-point grid and included the 6 topmost valence bands and 6 lowest conduction bands. In the plot of the optical spectra, we applied a Lorentzian broadening with an energy width of 120 meV. All *GW* and BSE calculations were performed with the BerkeleyGW package [4]. Representative RPA and BSE results at different doping levels are shown in Fig. S1. In all three cases, the most precise method to evaluate the rise of the e-h continuum for the direct excitations relies on the estimate of the *GW* direct quasiparticle gap (indicated by the dashed violet vertical line).

C. Doping dependence

To simulate the effects produced by a finite density of free carriers in the system, we performed BSE-*GW* calculations for electron doping values between 10^{-3} and 10^{-1} electrons per unit cell. This corresponds to electron dopings between 1.4×10^{19} cm^{-3} and 1.4×10^{21} cm^{-3}. The characteristic band structure of anatase TiO_2 ensures that electron doping of the conduction band can mimic the effects that photodoping of uncorrelated e-h pairs produces on the exciton response of the material. This can be observed in Fig. 1(a) of the main text. The top of the valence band in anatase TiO_2 is close to the X point of the Brillouin zone, whereas the bottom of the conduction band is at the Γ point. As such, the material is an indirect bandgap semiconductor. The single-particle states contributing to the exciton wavefunction are located along the Γ-Z symmetry line in the Brillouin zone, as indicated by the violet arrows. Photoexcitation of e-h pairs in our pump-probe experiments leads to

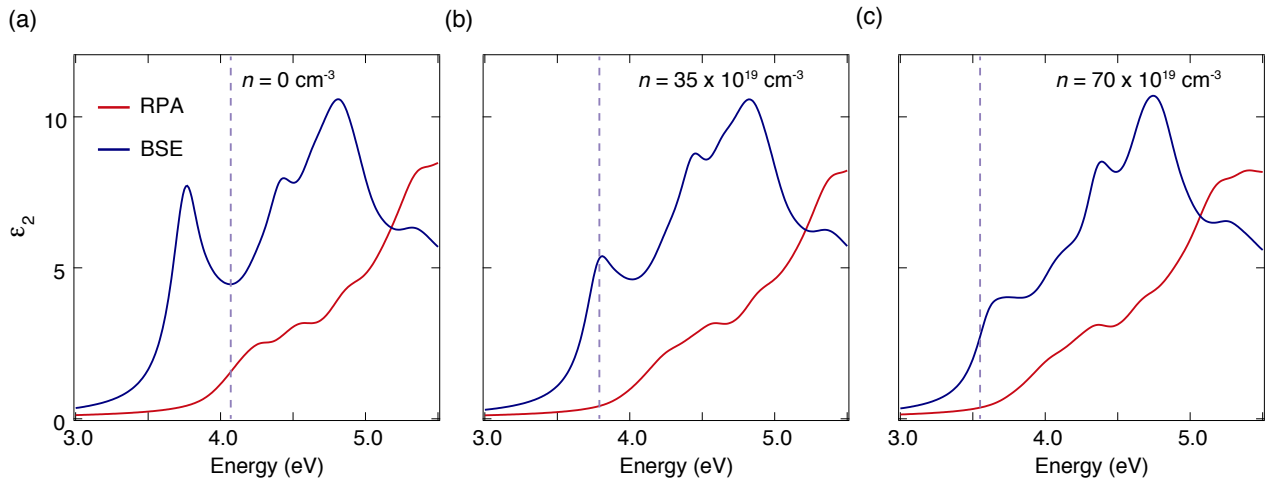

FIG. S1. Comparison between the imaginary part of the dielectric function of anatase TiO_2 calculated at the RPA-*GW* level (red lines) and that calculated at the BSE-*GW* level (blue lines). Three different dopings are shown: (a) $n = 0$ cm^{-3}; (b) $n = 35 \times 10^{19}$ cm^{-3}; (c) $n = 70 \times 10^{19}$ cm^{-3}. Only the inclusion of excitonic effects allows us to reproduce the experimental response. In addition, the RPA-*GW* spectrum signals the onset of the direct e-h continuum. Such an onset is also indicated by the direct quasiparticle gap computed at the *GW* level, which is represented by a dashed vertical line. The excitonic Mott transition occurs when the quasiparticle gap overlaps to the exciton peak energy and the excitons cease to be bound.

the rapid cooling of the electrons to the the conduction band minimum at Γ and of the holes to the top of the valence band at X. The effect of the free-carrier density on the exciton comes solely from the electron population at Γ. Thus, our calculations for *n*-doped TiO_2 provide a good account of the effects produced by the uncorrelated e-h pairs at time delays longer than the cooling time (> 50 fs).

D. Determination of the Mott transition

Here we describe how we estimate theoretically the exciton Mott density (n_M) of anatase TiO_2. For a semiconductor/insulator, n_M is defined as the carrier density at which the exciton binding energy (E_B) equals zero. Under these circumstances, the exciton is no longer bound and excitonic correlations can persist only in the form of resonant enhancements of the absorption spectrum.

We follow a rigorous approach to determine E_B. First, we calculate the single-particle band structure of the material at the *GW* level of theory for different values of the carrier density. Afterwards, we compute the exciton energy, E_{exc}, for each case by solving the BSE on top of the *GW* results, and identify the single-particle states contributing to the exciton. This allows us to estimate the value of the quasiparticle gap (E_{qp}) in the region of the Brillouin zone that builds up the exciton wavefunction. Finally, E_B is given by $E_{qp} - E_{exc}$. In Fig. 2(a), for each excess carrier density, E_{qp} is indicated by a vertical dashed line with the same color as the optical spectrum for that density. E_{exc} is simply the energy of the exciton peak in the spectrum. When $n = 0$ cm^{-3} (pristine anatase case in dark blue), E_B takes its largest value. As we increase n, E_B starts decreasing in value, and goes to zero for $n_M = 35 \times 10^{19}$ cm^{-3} (see Fig. 2(b) in the main text). Excitonic correlations persist even above n_M in the form of a resonant exciton [5].

II. SINGLE CRYSTAL GROWTH AND CHARACTERIZATION

High-quality single crystals of anatase TiO_2 were produced by a chemical transport method from anatase powder and NH_4Cl as transport agent, similar to the procedure described in Ref. [6]. In detail, 0.5 g of high-purity anatase powder were sealed in a 3 mm thick, 2 cm large and 20 cm long quartz ampoule together with 150 mg of NH_4Cl, previously dried at 60 °C under dynamic vacuum for one night, and 400 mbar of electronic grade HCl. The ampoule was placed in a horizontal tubular two-zone furnace and heated very slowly to 740 °C at the source, and 610 °C at the deposition zone. After two weeks, millimeter-sized crystals with a bi-pyramidal shape were collected and cut into rectangular bars (typically $0.8 \times 0.6 \times 0.15$ mm^3).

III. EXPERIMENTAL SET-UP

The ultrafast optical experiments were performed using a novel set-up of tunable UV pump and broad-

band UV probe, described in detail in Ref. [7]. A 20 kHz Ti:Sapphire regenerative amplifier (KMLabs, Halcyon + Wyvern500), providing pulses at 1.55 eV, with typically 0.6 mJ energy and around 50 fs duration, pumped a noncollinear optical parametric amplifier (NOPA) (TOPAS White - Light Conversion) to generate sub-90 fs visible pulses (1.77 - 2.30 eV range). The typical output energy per pulse was 13 μJ. Around 60% of the output of the NOPA was used to generate the narrowband pump pulses. The visible beam, after passing through a chopper, operating at 10 kHz and phase-locked to the laser system, was focused onto a 2 mm thick β-barium borate (BBO) crystal for nonlinear frequency doubling. The pump photon energy was controlled by the rotation of the crystal around the ordinary axis and could be tuned in a spectral range up to ∼0.9 eV (∼60 nm) wide. For our purpose, the pump photon energy was set at 4.10 eV, in order to selectively excite uncorrelated e-h pairs above the first excitonic peak of anatase TiO_2. The remaining NOPA output was used to generate the broadband UV probe pulses with ∼1.3 eV (∼100 nm) bandwidth through an achromatic doubling scheme.

To study the anatase TiO_2 single crystals, the set-up was used in the reflection geometry. The specimen was mounted on a rotating sample holder, in order to explore the transient reflectivity ($\Delta R/R$) along the desired crystalline axis. Pump and probe pulses, which have the same polarization, were focused onto the sample, where they were spatially and temporally overlapped. The spot size of the pump and the probe were 150 μm and 80 μm full-width at half-maximum (FWHM) respectively, resulting in a homogeneous illumination of the probed region. The portion of the probe beam reflected by the surface of the crystal was detected and the time evolution of the difference in the UV probe reflection with and without the pump pulse reconstructed. After the sample, the reflected probe was focused in a multi-mode optical fiber (100 μm), coupled to the entrance slit of a 0.25 m imaging spectrograph (Chromex 250is). The beam was dispersed by a 150 gr/mm holographic grating and imaged onto a multichannel detector consisting of a 512 pixel complementary metal-oxide-semiconductor (CMOS) linear sensor (Hamamatsu S11105, 12.5 × 250 μm pixel size) with up to 50 MHz pixel readout, so the maximum read-out rate per spectrum (almost 100 kHz) allowed us to perform shot-to-shot detection easily. The time resolution varied between 1 ps and 80 fs depending on the spectral coverage of the probe pulse. All the experiments were performed at room temperature.

IV. ESTIMATE OF THE PHOTOEXCITED CARRIER DENSITY

To explore the ultrafast optical response of TiO_2 single crystals in the high-density regime, it is crucial to accurately estimate the experimental e-h density, n_{e-h}, created by the pump pulse. This quantity can be expressed as

$$n_{e-h} = (1-R)\frac{F}{h\nu\lambda_{\mathrm{p}}}, \tag{1}$$

where F is the pump fluence, $h\nu$ is the pump photon energy, $\lambda_{\mathrm{p}} = 1/\alpha$ the light penetration depth in the material, and R is the reflectivity of the sample. All parameters are evaluated at the pump photon energy (4.10 eV). The uncertainty on n_{e-h} can be estimated by propagating the uncertainty in the variables entering Supplementary Equation (1), namely the absorption/reflection coefficients of the sample and the laser parameters. Moreover, as the choice of the excitation volume geometry is arbitrary, we discuss the approximations introduced for the calculation of the excitation spot size.

Absorption and reflection coefficients: The estimates of the absorption coefficient, as well as the amount of reflection from the sample surface, are based on measured data of spectroscopic ellipsometry, which is the most accurate experimental technique currently available to determine the real and imaginary parts of the dielectric function for any insulator above its optical energy gap. Our spectroscopic ellipsometry data are shown in Ref. [3] and the absorption/reflectance spectra are obtained directly from the measured optical quantities without the need of a Kramers-Kronig analysis. Since the error on the measured ellipsometry angles Ψ and Δ is less than 0.1%, the uncertainty in R, α, and λ_{p} remains well below 1%.

Incident laser fluence: The average incident laser fluence F (measured in μJ/cm^2) is defined as $F = P/(r \cdot A)$, where P is the average laser power, r the repetition rate of the laser system, and A the laser spot size. The impinging laser power P is measured accurately by using an ultraviolet-extended ultra-sensitive photodiode. For our photodiode, the uncertainty of the power measurement at a photon energy of 4.10 eV is equal to $\delta P = \pm 4\%$. The measurement of the spot size is performed using a camera-based beam profiling system consisting of a camera and analysis software. Here, the uncertainty in the width measurement is $\delta w = \pm 2\%$. Error propagation from w and P yields an uncertainty in the incident laser fluence of $\delta F = \sqrt{2\delta w + \delta P} \approx 5\%$.

Choice of the excitation volume: Although the uncertainty in n_{e-h} related to the laser parameters and absorption/reflection of the sample remains below 6%, an additional source of variation in the estimated e-h density originates from the arbitrary choice of the excitation volume. In agreement with the approach used in the literature, as excitation volume we consider a cylinder

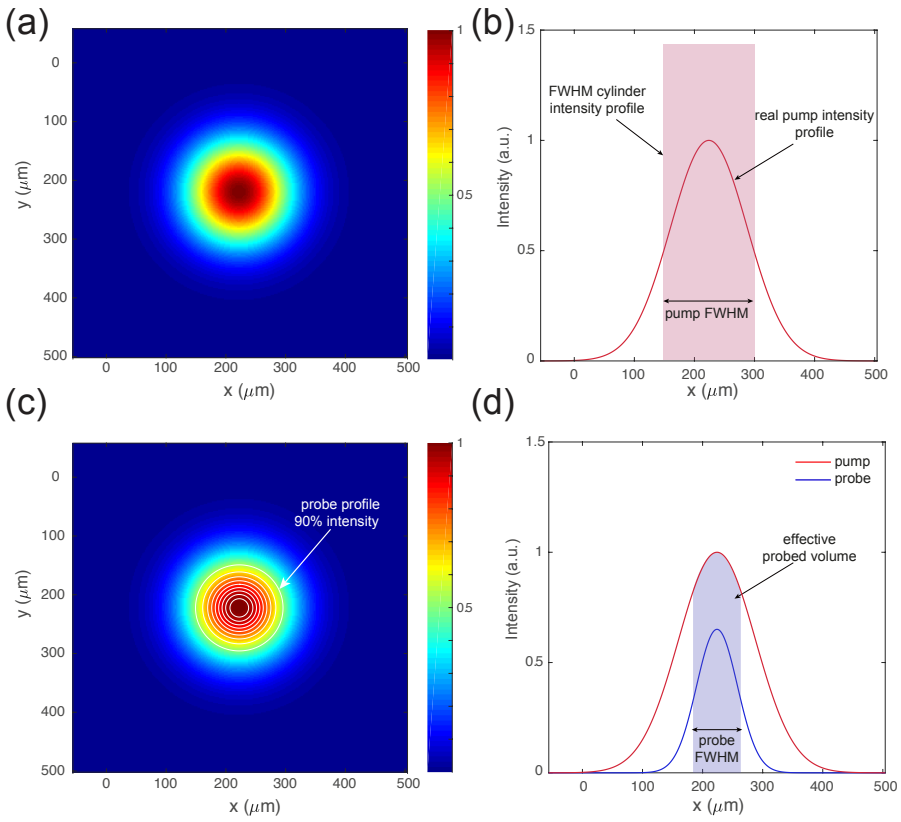

FIG. S2. (a) Simulation of the gaussian excitation beam used in our experiment (FWHM = 150 μm). (b) Profiles of the two-dimensional intensity distributions of the gaussian beam of panel (a) (red curve) and the one obtained by approximation of the gaussian beam with a cylinder. (c) Simulated gaussian intensity distributions of the pump (color-coded) and probe (white contour lines) beams used in the experiment. (d) Profiles of the two-dimensional intensity distributions of the pump and probe beams of panel (c), showing that in these experimental conditions the probed area coincides with the most intense part of the gaussian.

whose area A corresponds to the the laser spot size on the sample and whose height is equal to the light penetration depth λ_p (*i.e.*, the depth at which the intensity of the radiation is decreased by approximately $1/e = 37\%$ of its initial value). This choice of λ_p is justified by the similarity between the absorption coefficient of the pump and probe in the explored spectral range; thus, we can reasonably consider the same penetration depth for the pump and probe energies. On the other side, the choice of A deserves more attention. In Fig. S2(a), we simulate the gaussian excitation beam used in our experiment. Conventionally, the spot size diameter is approximated by the FWHM of the gaussian profile

$$A = \pi \left(\frac{\text{FWHM}}{2} \right)^2 , \tag{2}$$

Figure S2(b) shows the results of such an approximation by comparing the profiles of the two-dimensional intensity distributions of the gaussian beam (red curve) and the FWHM cylinder. In the former case, since the total intensity (*i.e.* the total volume under the gaussian surface) is contained in a smaller base, the avarage peak intensity is almost 1.5 times the peak intensity of the gaussian. However, the validity of this approximation depends on the relative size of the probe beam with respect to the pump, since a small probe will be able to probe *locally* the photoexcited surface and provide a more precise estimate of the e-h density. This concept is illustrated in Figs. S2(c,d), where we compare the simulated profiles of the pump and probe beams used in the experiment. When the two laser beams are perfectly overlapped, being the probe much narrower than the pump, the probed area will coincide with the most intense part of the gaussian, whose intensity is almost 1.5 times smaller than the one resulting from the FWHM approximation. With the latter being the approximation we use in our study, the declared excitation densities may exceed the actual densities by a factor 1.5-2.

Therefore, by considering all sources of uncertainty presented above, we conclude that the densities reported in our study will differ from the actual densities by a factor no greater than 1.5-2. Such an uncertainty does not

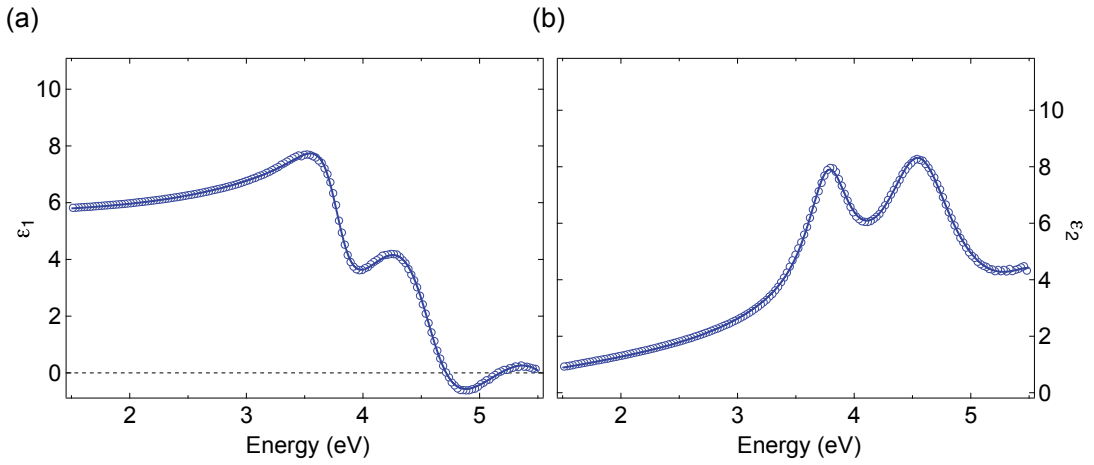

FIG. S3. (a) Real ($\epsilon_1(\omega)$) and (b) imaginary ($\epsilon_2(\omega)$) parts of the complex dielectric function of anatase TiO_2, measured at room temperature with spectroscopic ellipsometry (blue dots) along the crystallographic a-axis. Solid blue lines show the simultaneous fits of both measured data set to the same Lorentz model.

influence the discussion and conclusion of our paper.

V. LINESHAPE ANALYSIS

In this Section, we describe the lineshape analysis performed to track the relevant exciton parameters in our pump-probe experiment. As a first step, we modeled the steady-state complex dielectric function with a set of Lorentz oscillators. The real ($\epsilon_1(\omega)$) and imaginary ($\epsilon_2(\omega)$) parts of the dielectric function were measured directly with spectroscopic ellipsometry [3]. Figure S3(a,b) shows the experimental traces (blue dotted lines) and the results of the Lorentz model (blue solid lines), indicating the accuracy of our fit. The fit function comprises four Lorentz oscillators (accounting for the indirect gap transition at 3.53 eV, the bound exciton at 3.77 eV, the resonant exciton at 4.55 eV, and an interband transition that captures the high-energy response), as well as a background tail due to defect-assisted transitions and residual scattered light from surface inhomogeneities. Figure S4 displays the decomposition of the $\epsilon_2(\omega)$ spectrum into the different Lorentzian contributions. Next, we used the modeled $\epsilon_1(\omega)$ and $\epsilon_2(\omega)$ to determine the reflectivity $R(\omega)$ using standard electrodynamical formulas [8]. The final result was compared to the experimental reflectivity spectrum $R(\omega)$. The latter was also determined by combining the experimental $\epsilon_1(\omega)$ and $\epsilon_2(\omega)$ measured by ellipsometry. The accuracy of the fit can be observed in Fig. 1(b) in the main text.

Once this model of the steady-state optical response was established, we combined the steady-state data of $R(\omega)$ with the time-resolved reflectivity (ΔR/R(ω,t)) measured in this work, following a well-known procedure in the context of ultrafast broadband optical spectroscopy [9–11]. We remark that the static $R(\omega)$ was measured in the broad spectral range 1.0-5.5 eV, while $\Delta R/R(\omega$,t) was monitored by our ultrafast experiment in the 3.6-4.4 eV region. Combining these two quantities allowed us to obtain the momentary reflectivity $R(\omega, t)$ in the range covered by the pump-probe experiment by multiplying ($\Delta R/R(\omega, t) + 1$) at a fixed time delay t by $R(\omega)$ itself. These are the raw data shown in Fig. 3(b) of the main text. Finally, to determine the momentary absorption $\alpha(\omega, t)$, we iterated the Lorentz fit at all measured time delays, using as starting parameters those describing the steady-state $R(\omega)$ of Fig. 1(b) and letting only the Lorentz oscillator representing

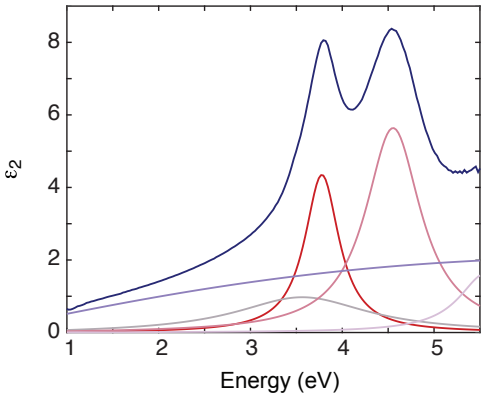

FIG. S4. Decomposition of the $\epsilon_2(\omega)$ data (blue lines) into the separate Lorentz oscillators used in our model. The final fit is shown in Fig. S3.

the bound exciton free to vary. This was sufficient to reproduce the spectra at all time delays. The choice of letting only the bound exciton free to vary is justified by the fact that the pump excitation induces a very small modification of the reflectivity, depleting the optical spectral weight only around this exciton. The depleted spectral weight is eventually transferred to very low energies (i.e. mostly the terahertz range) in the form of free-carrier absorption [12]. This procedure allowed us to retrieve all the optical quantities of interest using the standard electrodynamical formulas [8], among which the $\alpha(\omega$,t) spectrum presented in Fig. 3(c), as well as the evolution of the bound exciton parameters (Fig. 3(d-f)).

VI. HIGH TIME RESOLUTION DATA

We also performed high-precision measurements of $\Delta R/R(\omega, t)$ in a narrower spectral range around the exciton peak (3.72 - 4.20 eV) with a time resolution of 80 fs. The pump fluence is the same as that used in the pump-probe experiment with 700 fs time resolution. Figure S5(a) shows normalized temporal traces selected at representative probe photon energies. Although the response was measured up to 20 ps, here we just display the first ps of dynamics. We observe a resolution-limited rise of the response in the low-energy region of the spectrum, followed by a fast relaxation component that is prominent around 3.95 eV. Figure S5(b) displays the momentary reflectivity $R(\omega, t)$ before photoexcitation (blue curve) and at a time delay of 120 fs (red curve). At 120 fs, we observe the persistence of the bound exciton feature, which becomes broader due to the larger long-range Coulomb screening caused by the photoexcited uncorrelated e-h pairs (note that the wiggles that are visible on the signal are due to noise). The fact that the exciton broadens implies a substantial modification of the exciton coherence lifetime, but not of the exciton E_B. As such, the estimated photoexcitation density represents a lower bound to the nominal n_M in anatase TiO_2.

VII. RELEVANCE OF THE HIGH MOTT DENSITY IN ANATASE TIO_2

In this Section, we describe the importance of our results in relation to fundamental and applied research. Fundamentally, a large n_M is a prerequisite for the creation of room temperature exciton-polaritons when the system is placed inside a microcavity. This has been explored in the case of Wannier excitons of low-dimensional semiconductor nanostructures [34] and in the context of Frenkel excitons in molecular systems [35, 36]. In anatase TiO_2, the excitons are characterized by large oscillator strength, small dephasing due to population relaxation

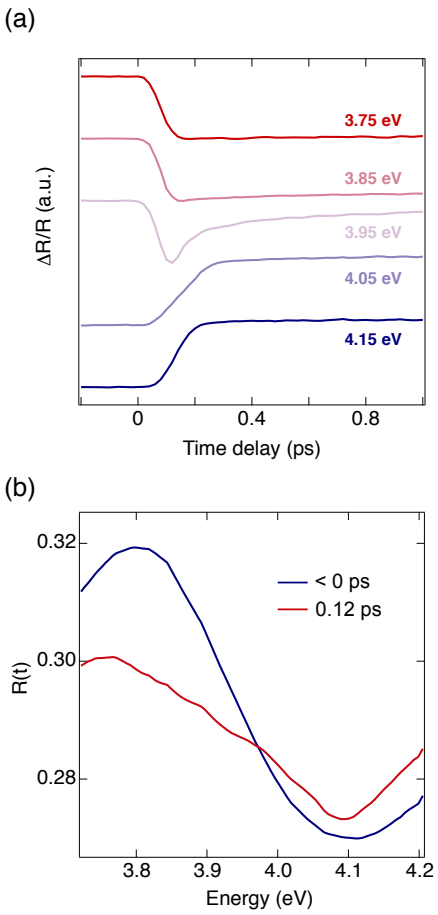

FIG. S5. (a) High-time resolution ΔR/R temporal traces selected at representative photon energies, as indicated in the labels. For clarity, the traces are normalized, vertically shifted, and displayed in the first ps of response. (b) Comparison between the momentary reflectivity $R(\omega, t)$ before and after photoexcitation.

into e-h pairs, and high n_M. These aspects together would allow the realization of stable exciton-polaritons in high-quality thin films of TiO_2 embedded in optical cavities and open the avenue to the study of possible condensation phenomena and nonlinear polariton-polariton interactions.

Technologically, a high n_M ensures that the excitons are very stable quasiparticles even in the presence of the large carrier densities involved in many applications. One of these applications is photocatalysis, in which anatase TiO_2 represents one of the most used platforms at room temperature [37]. It has been proposed that the excitons of anatase TiO_2 may allow for an efficient transfer of energy to the reaction centers at the (001) surfaces of conventionally-used TiO_2 nanoparticles [38]. The presence of a large n_M ensures that the exciton population survives even in the presence of many thermally-activated carriers (owing to defects and impurities) in these highly-

Material	E_B (meV)	n_M (cm^{-3})	Temperature (K)	Reference
Anatase TiO_2	> 150	$> 5 \times 10^{19}$	295 K	This work
ZnO	60	0.8-6.4 $\times 10^{18}$	295 K	[13–15]
$CH_3NH_3PbBr_3$	70	8×10^{17}	295 K	[11]
GaAs	4.2	1.2-1.8 $\times 10^{16}$	49 K	[16]
GaN	26	1×10^{18}	10 K	[17]
Diamond	80	3×10^{18}	295 K	[18]
Cu_2O	150	3×10^{18}	10 K	[19, 20]
Si	15	7×10^{17}	295 K	[21–23]
Ge	4.2	1×10^{16}	8 K	[24]
ZnTe	12.7	3×10^{17}	20 K	[25, 26]
ZnS	36-40	1.9×10^{17}	2 K	[27]
ZnSe	19-20	0.1-5 $\times 10^{17}$	2-295 K	[27, 28]
CdS	28	2.6-50 $\times 10^{17}$	2-295 K	[29, 30]
CdSe	15	1×10^{17}	80 K	[31, 32]
CdTe	24.8	3×10^{18}	295 K	[33]

TABLE S1. Exciton Mott densities in three-dimensional band semiconductors.

defective nanoparticles. Another application in which anatase TiO_2 is widely used is that of transparent conducting substrates. The conductivity of these substrates stems from the transport of thermally-activated electrons (owing to the presence of donor states, such as oxygen vacancies or Nb/Ta substitutions) [39, 40]. Revealing that TiO_2 has such a high n_M can also guide the rational design of the carrier density needed to optimize the transparency window of these substrates (by choosing densities above n_M, at which the bound exciton peak disappears and the material is more transparent).

VIII. COMPARISON WITH OTHER MATERIALS

In this Section, we compare the results obtained on anatase TiO_2 with those of band insulators (i.e. devoid of strong electron-electron correlations) known in the literature. To establish an accurate comparison, we consider bulk solids characterized by a three-dimensional electronic structure and whose exciton states are electric dipole-allowed and built up from the mixing of single-particle transitions between the valence and the conduction bands. Hence, we do not include quasi-two dimensional materials (*e.g.*, transition metal dichalcogenides), confined nanostructures, as well as bulk solids with Frenkel excitons arising from localized states (*e.g.*, $d-d$ transitions in transition metal oxides with partially-filled d orbitals). To account for all the materials explored in the literature, in providing the estimated n_M we do not make any distinction between chemically-doped and photo-doped systems, although the Mott transition assumes a different meaning in the two classes of systems (see Ref. [41] for details). The complete list is shown in Table S1. Some of the materials considered here host excitons with low values of E_B and therefore the estimate of n_M had to be performed at low temperature. In contrast, other solids have strongly bound excitons and n_M is evaluated at room temperature. We observe that anatase TiO_2 has the largest n_M, i.e. at least one order of magnitude higher than that exhibited by other band semiconductors. As indicated in the main text, we ascribe this phenomenon to the interplay between the large E_B and the small impact of bandgap renormalization when an excess carrier density is injected in the solid (either through chemical- or photo-doping).

[1] L. Hedin, Phys. Rev. **139**, A796 (1965).
[2] G. Onida, L. Reining, and A. Rubio, Rev. Mod. Phys. **74**, 601 (2002).
[3] E. Baldini, L. Chiodo, A. Dominguez, M. Palummo, S. Moser, M. Yazdi-Rizi, G. Auböck, B. P. P. Mallett, H. Berger, A. Magrez, C. Bernhard, M. Grioni, A. Rubio, and M. Chergui, Nat. Commun. **8**, 13 (2017).
[4] J. Deslippe, G. Samsonidze, D. A. Strubbe, M. Jain, M. L. Cohen, and S. G. Louie, Comp. Phys. Commun. **183**, 1269 (2012).
[5] E. Baldini, A. Dominguez, L. Chiodo, E. Sheveleva, M. Yazdi-Rizi, C. Bernhard, A. Rubio, and M. Chergui, Phys. Rev. B **96**, 041204 (2017).
[6] H. Berger, H. Tang, and F. Levy, J. Crys. Growth **130**, 108 (1993).
[7] G. Auböck, C. Consani, F. van Mourik, and M. Chergui, Opt. Lett. **37**, 2337 (2012).
[8] M. Dressel and G. Grüner, "Electrodynamics of Solids: Optical Properties of Electrons in Matter," (2002).
[9] B. Mansart, M. J. G. Cottet, T. J. Penfold, S. B. Dugdale, R. Tediosi, M. Chergui, and F. Carbone, Proc. Natl. Acad. Sci. **109**, 5603 (2012).
[10] F. Novelli, D. Fausti, J. Reul, F. Cilento, P. H. Van Loosdrecht, A. A. Nugroho, T. T. Palstra, M. Grüninger, and F. Parmigiani, Phys. Rev. B **86**, 165135 (2012).
[11] T. Palmieri, E. Baldini, A. Steinhoff, A. Akrap, M. Kollár, E. Horváth, L. Forró, F. Jahnke, and M. Chergui, Nat. Commun. **11**, 850 (2020).

[12] H. Matsuzaki, Y. Matsui, R. Uchida, H. Yada, T. Terashige, B.-S. Li, A. Sawa, M. Kawasaki, Y. Tokura, and H. Okamoto, J. Appl. Phys. **115**, 053514 (2014).

[13] C. Klingshirn, R. Hauschild, J. Fallert, and H. Kalt, Phys. Rev. B **75**, 115203 (2007).

[14] M. A. M. Versteegh, T. Kuis, H. T. C. Stoof, and J. I. Dijkhuis, Phys. Rev. B **84**, 035207 (2011).

[15] A. Schleife, C. Rödl, F. Fuchs, K. Hannewald, and F. Bechstedt, Phys. Rev. Lett. **107**, 236405 (2011).

[16] A. Amo, M. Martín, L. Viña, A. Toropov, and K. S. Zhuravlev, Phys. Rev. B **73**, 035205 (2006).

[17] C. K. Choi, Y. H. Kwon, J. S. Krasinski, G. H. Park, G. Setlur, J. J. Song, and Y. C. Chang, Phys. Rev. B **63**, 115315 (2001).

[18] M. Nagai, R. Shimano, K. Horiuch, and M. Kuwata-Gonokami, Phys. Status Sol. (b) **238**, 509 (2003).

[19] G. Manzke, D. Semkat, F. Richter, D. Kremp, and K. Henneberger, in *J. Phys. Conf. Ser.*, Vol. 210 (IOP Publishing, 2010) p. 012020.

[20] J. Heckötter, M. Freitag, D. Fröhlich, M. Aßmann, M. Bayer, P. Grünwald, F. Schöne, D. Semkat, H. Stolz, and S. Scheel, Phys. Rev. Lett. **121**, 097401 (2018).

[21] P. P. Altermatt, J. Schmidt, G. Heiser, and A. G. Aberle, J. Appl. Phys. **82**, 4938 (1997).

[22] R. Hull, *Properties of Crystalline Silicon*, 20 (IET, 1999).

[23] M. A. Green, AIP Advances **3**, 112104 (2013).

[24] F. Sekiguchi and R. Shimano, Phys. Rev. B **91**, 155202 (2015).

[25] F. Majumder, H. Kalt, C. Klingshirn, H. Stanzl, and W. Gebhardt, Phys. Stat. Sol. (b) **188**, 191 (1995).

[26] Y.-M. Yu, S. Nam, K.-S. Lee, Y. D. Choi, and B. O, J. Appl. Phys. **90**, 807 (2001).

[27] A. Manar, A. Chergui, D. Guennani, D. Ohlmann, T. Cloitre, and R. L. Aulombard, Mater. Sci. Eng. B **43**, 121 (1997).

[28] D. Semkat, F. Richter, D. Kremp, G. Manzke, W.-D. Kraeft, and K. Henneberger, Phys. Rev. B **80**, 155201 (2009).

[29] F. Henneberger, U. Woggon, J. Puls, and C. Spiegelberg, Appl. Phys. B **46**, 19 (1988).

[30] C. Fricke, R. Heitz, A. Hoffmann, and I. Broser, Phys. Rev. B **49**, 5313 (1994).

[31] J. G. Fujimoto, S. G. Shevel, and E. P. Ippen, Sol. State Comm. **49**, 605 (1984).

[32] O. Maksimov, M. Muñoz, and M. Tamargo, Microelectron. J. **37**, 19 (2006).

[33] S. Z. Karazhanov, Y. Zhang, A. Mascarenhas, and S. Deb, J. Appl. Phys. **87**, 8786 (2000).

[34] H. Deng, G. Weihs, C. Santori, J. Bloch, and Y. Yamamoto, Science **298**, 199 (2002).

[35] J. D. Plumhof, T. Stöferle, L. Mai, U. Scherf, and R. F. Mahrt, Nat. Mater. **13**, 247 (2014).

[36] K. S. Daskalakis, S. A. Maier, R. Murray, and S. Kéna-Cohen, Nat. Mater. **13**, 271 (2014).

[37] A. Fujishima and K. Honda, Nature **238**, 37 (1972).

[38] D. Varsano, G. Giorgi, K. Yamashita, and M. Palummo, J. Phys. Chem. Lett. **8**, 3867 (2017).

[39] Y. Furubayashi, T. Hitosugi, Y. Yamamoto, K. Inaba, G. Kinoda, Y. Hirose, T. Shimada, and T. Hasegawa, Appl. Phys. Lett. **86**, 252101 (2005).

[40] T. Hitosugi, Y. Furubayashi, A. Ueda, K. Itabashi, K. Inaba, Y. Hirose, G. Kinoda, Y. Yamamoto, T. Shimada, and T. Hasegawa, Jpn. J. Appl. Phys. **44**, L1063 (2005).

[41] D. Snoke, Solid State Comm. **146**, 73 (2008).